

Soft X-ray Absorption Spectroscopic Analysis for Reaction Mechanism of Rechargeable Batteries

Yuki Orikasa¹, Toshiaki Ohta²

1) College of Life Sciences, Ritsumeikan University, 1-1-1 Noji-Higashi, Kusatsu, 525-8577, Japan

2) Research Organization of Science & Engineering, Ritsumeikan University, 1-1-1 Noji-Higashi, Kusatsu 525-8577, Japan

Abstract

Soft X-ray absorption spectroscopy (SXAS) is one of powerful tool to characterize the electronic structure for analysis of rechargeable battery. This review introduces the recent studies of the battery electrode and electrolyte using SXAS in Ritsumeikan SR center. In the introduction, the advantage of SXAS is explained. Then, after overviewing the previous X-ray absorption spectroscopic study using the conventional cathode material, LiNiO_2 , the charge compensation mechanism related in lithium-rich layered cathode material, $\text{Li}_{1.16}\text{Ni}_{0.15}\text{Co}_{0.19}\text{Mn}_{0.50}\text{O}_2$ is discussed. To measure *operando* X-ray absorption near edge structure at soft X-ray region, originally designed measurement cell has been developed, which is utilized to the analysis of nonequilibrium phenomena during battery reaction. SXAS detects the surface state on electrode materials, which has been applied to the analysis of surface degradation on LiCoO_2 cathode. SXAS in SR center has also contributed on the analysis of next-generation rechargeable battery. Cathode materials newly developed for magnesium rechargeable batteries and potassium batteries were measured, which indicated the charge/discharge reaction contributing the ligand-hole state. Analysis of liquid electrolyte for magnesium rechargeable batteries was performed. These SXAS measurements have an important role to characterize the unknow phenomena during laboratory studies on battery reaction.

1. Introduction

Rechargeable batteries such as lithium-ion batteries are not only utilized as a portable power source for laptops and smartphones but are also expected to be utilized as a large-scale energy storage in electric vehicles and grids for promoting carbon neutrality. The fundamental reaction in rechargeable batteries is an electrochemical reduction-oxidation (redox) reaction of cathode and anode active materials which involves electron transfer between electrode and electrolyte. To improve the battery performance, such as high energy density, durability and safety, it is necessary to understand the reaction mechanism of electrode active materials for charge/discharge. This is because the charge/discharge capacity is mainly limited by the reduction-oxidation reaction of the active materials in rechargeable batteries. For the analysis of the redox reaction caused in electrode active materials, soft X-ray absorption spectroscopy (SXAS) is a powerful tool to provide the essential knowledge related to the electronic structure of redox sites (Fig. 1). This review will cover the reaction analysis using SXAS of lithium-ion batteries and next-generation batteries performed in Ritsumeikan SR center based on the published literatures.¹⁻⁴

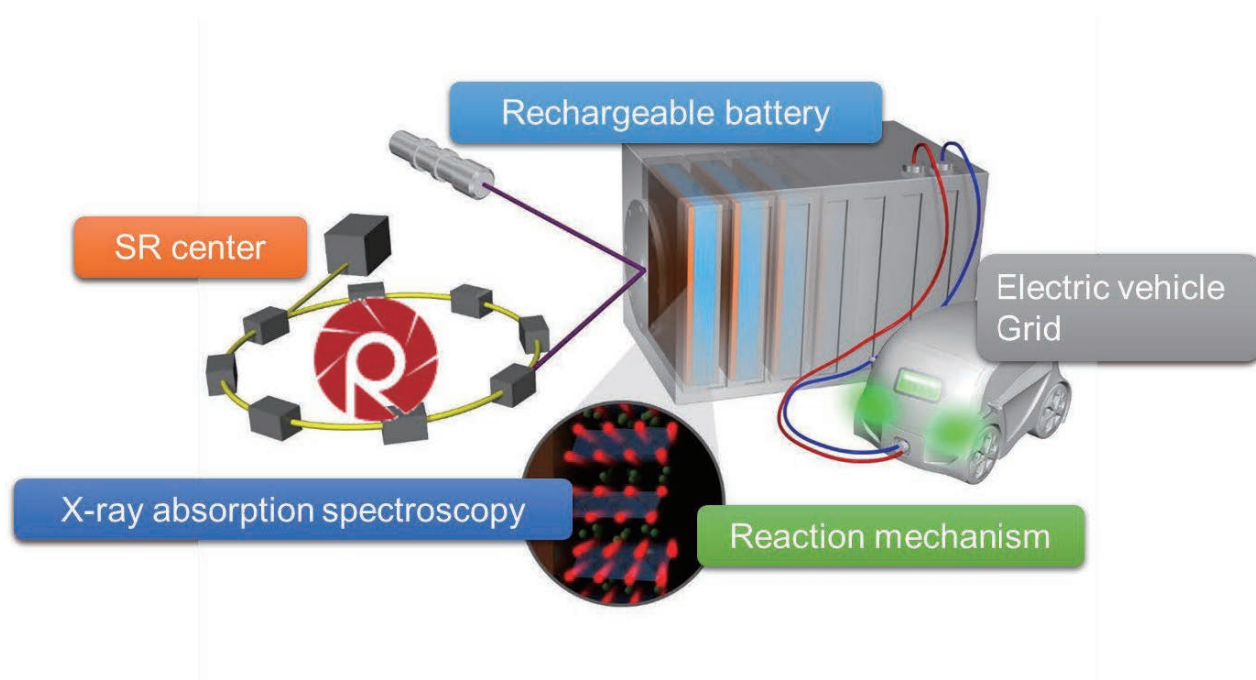


Fig. 1 Schematic illustration for analysis of battery reaction by means of soft X-ray absorption spectroscopy in Ritsumeikan SR center.

2. Lithium-ion battery

In a commonly used lithium-ion battery, lithium transition-metal oxide such as LiCoO_2 is mainly used as a cathode active material.⁵ In the case of the 3d transition-metal oxides, the

charge neutral condition after insertion and de-insertion of lithium ions seems to be maintained by the redox reaction of the transition metal. Actual electron transfer is contributed by the hybridized 3d orbital of the transition metal and 2p orbital of oxygen.⁶ To realize more redox reactions, X-ray absorption near edge structure (XANES) of the transition-metal L-edge and oxygen K-edge, which can directly show these electronic structures near the Fermi level, have been discussed.⁷ When the charge reaction of LiNiO_2 cathode proceeds, the Ni K-edge XANES is shifted toward high energy.⁸ However, this phenomenon is due to the change in the 1s orbital, and there is little information about the electron transfer in the outermost shell. XANES spectra of Ni L- and O K-edges measured in *ex situ* conditions after charging were reported.⁹ While the Ni L-edge spectrum is unchanged at the early stage of charging, the change in the peak intensity at the O K-edge is large. The observed pre-edge peak is originated from the hybridization of Ni 3d and O 2p orbitals, indicating that the redox reaction of nickel (change in the oxidation number of Ni) alters the electronic structure change of the hybridized orbital of nickel and oxygen to maintain charge-neutral conditions.

Recently, cathode materials with a high capacity using anion redox have been devised, and interesting charge–discharge properties have been reported in which only valence changes of transition metals cannot be explained.¹⁰⁻¹⁴ It is important to clarify the electronic structure changes of active materials, especially the electronic structure change of anions such as oxide ions, for the material design of next-generation high-capacity cathode materials. Oishi et al. performed an electronic structure analysis of Li_2MnO_3 and Li-excess layer oxides using XANES in the soft X-ray range, showing that an oxide ion contributes to charge compensation at high potential.¹⁵⁻¹⁷ Figure 2 shows Ni, Co and Mn $L_{\text{II,III}}$ -edge XANES of charged and discharged $\text{Li}_{1.16}\text{Ni}_{0.15}\text{Co}_{0.19}\text{Mn}_{0.50}\text{O}_2$ measured in a total electron yield mode and partial fluorescence mode.¹⁷ The contribution for the charge compensation during charge/discharge by each 3d metal orbital can be discussed. The clear structure change observed in Ni $L_{\text{II,III}}$ -edge represents the redox reaction of $\text{Ni}^{2+}/\text{Ni}^{4+}$ contributes the charge/discharge reaction. The weak change in Co $L_{\text{II,III}}$ -edge implies the effect of the hybridization between Co 3d and O 2p orbitals. On the other hand, Mn $L_{\text{II,III}}$ -edge XANES shows almost no change, indicating no contribution to the charge compensation of Mn 3d orbital for charge/discharge. However, the hybridization state contributed by Ni, Co, Mn and O has an important role for high charge/discharge capacity. Figure 3 shows O K-edge XANES of charged and discharged $\text{Li}_{1.16}\text{Ni}_{0.15}\text{Co}_{0.19}\text{Mn}_{0.50}\text{O}_2$ measured in a total electron yield mode and partial fluorescence mode.¹⁷ After charge, the peak width is spread towards lower energy indicating the arrow 1. This is related to the formation of oxygen hole to maintain the charge-neutral conditions for charge reaction.

Another representative structure change is observed showing as the arrow 2. The peak formation at high energy side corresponds to the newly formed orbital which is proposed in the later reports.^{18, 19}

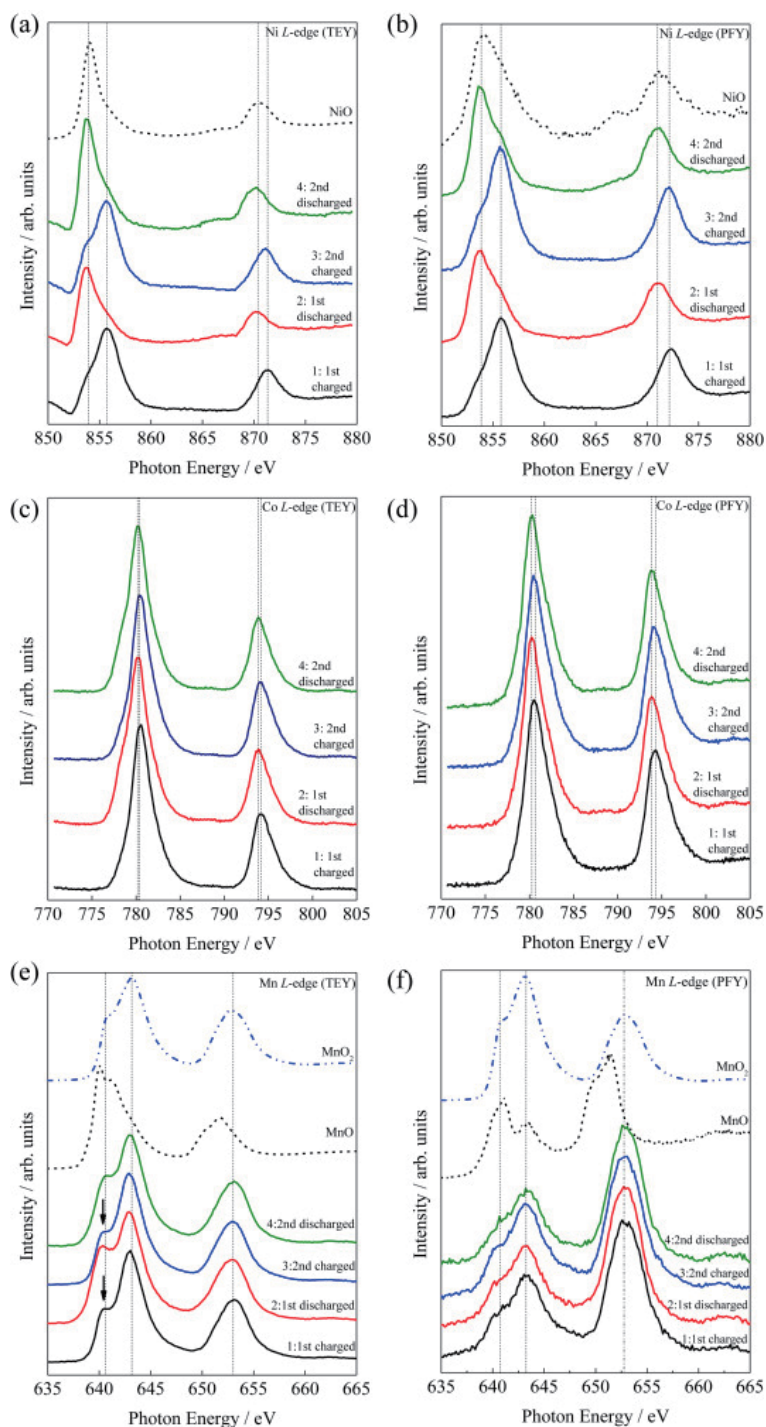


Fig. 2 Metal $L_{II,III}$ -edge XANES of the charged and discharged $\text{Li}_{1.16}\text{Ni}_{0.15}\text{Co}_{0.19}\text{Mn}_{0.50}\text{O}_2$ for the reversible 1st and 2nd cycle processes. (a) Ni in TEY mode, (b) Ni in PFY mode, (c) Co in TEY mode, (d) Co in PFY mode, (e) Mn in TEY mode and (f) Mn in PFY mode.

Reprinted from Ref. 16, Copyright (2015), with permission from Elsevier.

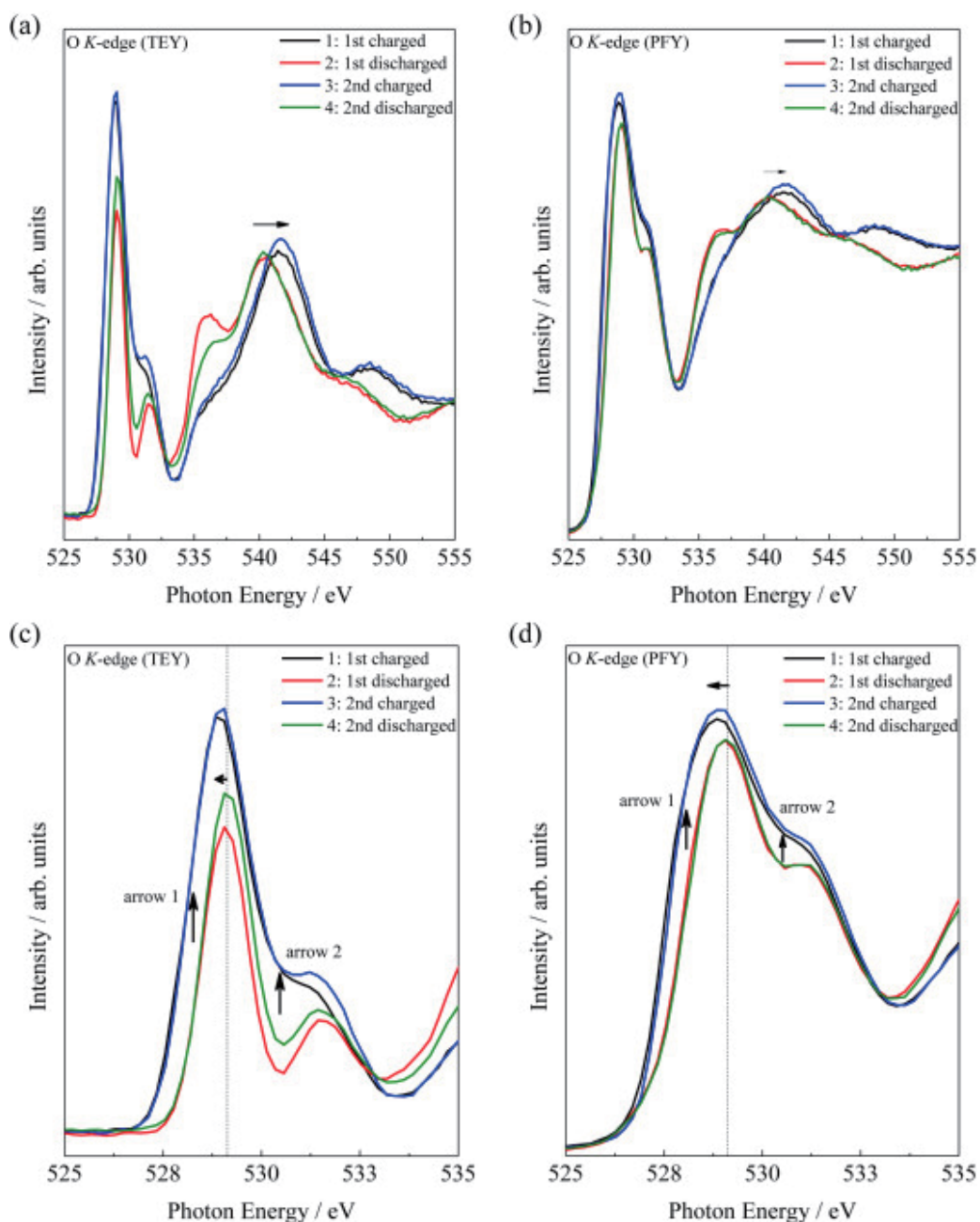


Fig. 3 O K-edge XANES of the charged and discharged $\text{Li}_{1.16}\text{Ni}_{0.15}\text{Co}_{0.19}\text{Mn}_{0.50}\text{O}_2$ for the reversible 1st and 2nd cycle processes. They are obtained in (a) TEY and (b) PFY mode. The pre-edge structures are expanded in (c) TEY and (d) PFY mode. Reprinted from Ref. 16, Copyright (2015), with permission from Elsevier.

Yabuuchi et al. used the O K-edge XANES to investigate the "superoxide states" of cathode materials $\text{Li}_{1.3}\text{Nb}_{0.3}\text{Mn}_{0.4}\text{O}_2$ and $\text{Li}_{1.2}\text{Ti}_{0.4}\text{Mn}_{0.4}\text{O}_2$, which differ from conventional materials in their charge process.^{14, 20} These XAS measurements were performed using

samples after cell disassembly and washing without air exposure. The redox reaction of oxide ions occurs mainly on the high potential side during the charge–discharge process in a nonequilibrium state. Therefore, *operando* measurements performed under actual cell-operating conditions while irradiating X-rays are useful for elucidating the reaction mechanisms.

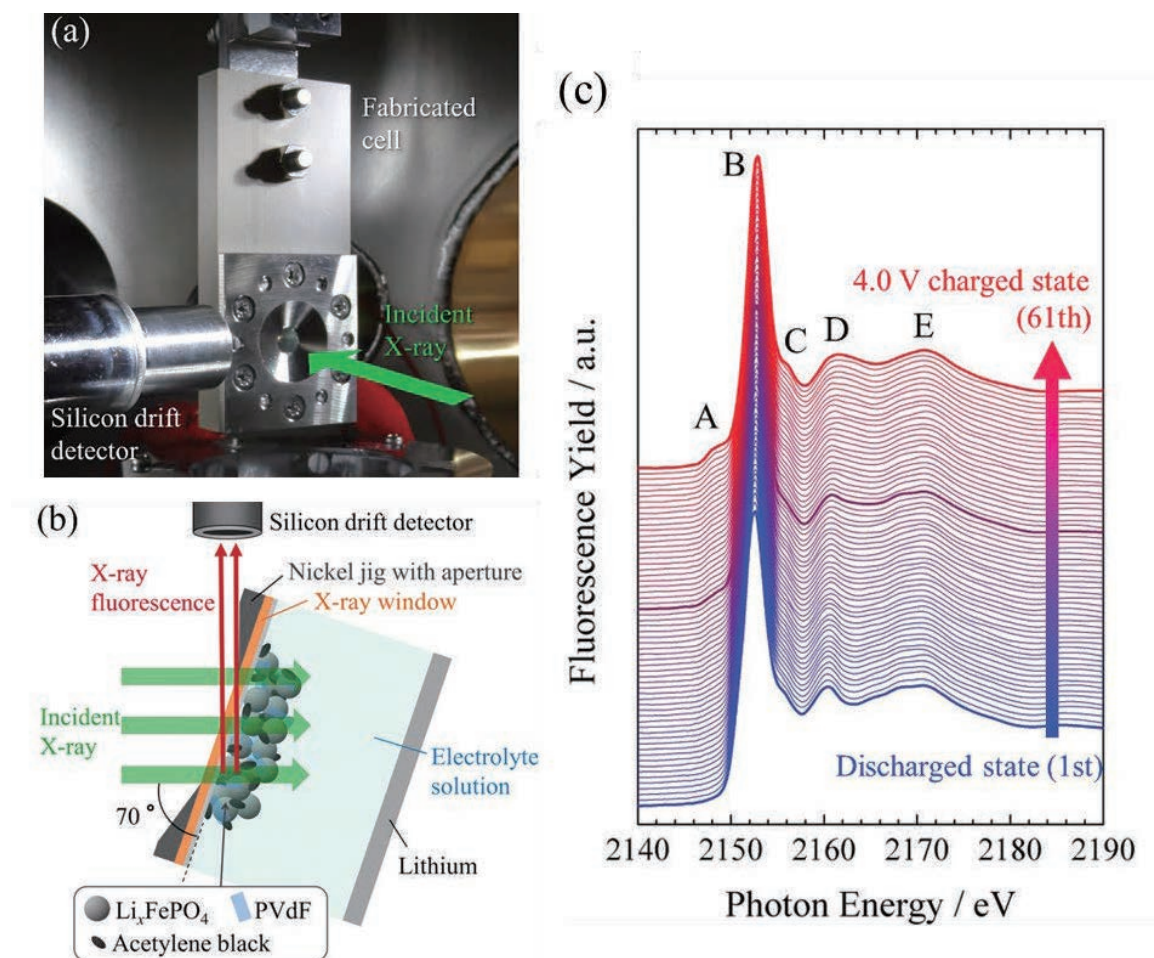


Fig. 4 Experimental setup for *in situ* TX-XAS measurement.²¹ (a) Photograph in the high vacuum sample chamber. (b) Schematic top view. (c) Observed P K-edge XANES of the LiFePO_4 composite electrode in the charging process recorded with the PFY mode. (a) Series of XAS spectra with fixed vertical offsets. Discharged state (1st), After 110 min (35th), and 4.0 V charged state (61th) are drawn by thick lines, respectively. Reprinted from Ref. 21, Copyright (2014), with permission from Elsevier.

Compared to the hard X-ray region measurable in the atmosphere, in the soft X-ray region of 3000 eV or less, the measurement environment is largely constrained, and it is difficult to directly apply the cell as described above. In particular, no liquid electrolyte is available for measurement in a vacuum chamber. For this reason, a unique cell structure has been proposed in which cell components are separated between a vacuum and an

atmospheric environment by using a window material through which X-rays penetrate.²¹ As shown in Fig. 4(a) and (b), the electrode-coated window and the electrolyte are placed in a sealable cell, which is brought into a vacuum chamber and irradiated with X-rays through the window to detect fluorescence X-rays. Using a SiN window enables the measurement of the P K-edge XANES spectrum of LiFePO_4 electrode material during the charge–discharge reaction using liquid electrolyte (Fig. 4(c)).

Using the *operando* measurement cell, O K-edge XANES spectra of $\text{Li}_{1.2-x}\text{Ti}_{0.4}\text{Mn}_{0.4}\text{O}_2$ during the initial charge process were analyzed, which was measured in Spring-8 due to the requirement of high brightness.²² The pre-edge peak shifted toward lower energy in the initial stage of charging ($x < 0.38$), after which a new peak appeared ($x > 0.38$). Because Mn L-edge XANES spectra show no change during the middle and later stages of charging ($x > 0.38$), the change in the O K-edge XANES is attributed to the rehybridization of the 3d-2p orbitals of the Mn-O bond with the oxidation of Mn ($x < 0.38$), and the change after $x = 0.38$ is attributed to the charge compensation with oxide ions. The electronic structure between the transition metal and oxygen is a key point for the charge-compensation mechanism, and material design using oxygen redox is required while suppressing the release of oxygen gas.²²

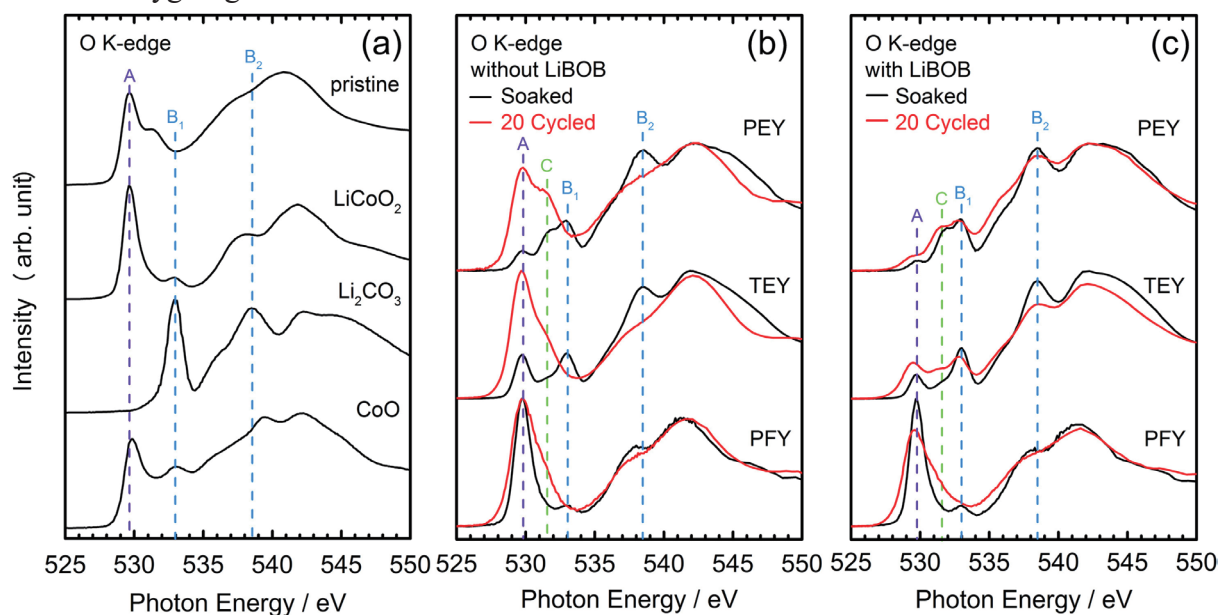


Fig. 5 O K-edge XANES of (a) the pristine electrode, LiCoO_2 , Li_2CO_3 , CoO powders, (b) the soaked- and 20 cycled- LiCoO_2 electrodes in the electrolyte without, and (c) with 0.1 wt% LiBOB. Reprinted from Ref. 23, Copyright (2014), with permission from Elsevier.

SXAS is also used for the analysis of surface products of lithium-ion battery positive electrode materials. Fig. 5 compares O-K XANES after cycling of the charge-discharge response of the LiCoO_2 positive electrode with the addition of lithium bis(oxalate) borate

(LiBOB) additives to the electrolyte.²³ Spectra obtained by the electron-yield method show that after cycling without LIBOB, the spectra derived from degraded surface-products are dominant structures. However, when LIBOB is added, it can be confirmed that the surface-product is suppressed. By discussing XANES of Li K-edge and C K-edge together, surface state for lithium-ion battery cathode materials can be analyzed.

3. Next-generation rechargeable battery

Since magnesium metal has a high theoretical gravimetric and volumetric capacities and exhibits a negative standard electrode potential, rechargeable batteries using magnesium metal as a negative electrode is expected to exhibit high energy density. Electrochemical insertion and de-insertion reactions of magnesium ion are much slower than that of lithium ions when the same host structure is applied. To solve the above problems, various cathode materials typified by inorganic transition metal sulfides and oxides have been studied so far. The representative materials showing reversible cycling are the chalcogenides like Chevrel-type compounds.²⁴ Oxides such as spinel has a problem in reversibility due to disproportionation reaction and conversion reaction during charge/discharge.²⁵

To ensure diffusion paths of magnesium ion in crystal structure, structural design of polyanionic compounds with multidimensional diffusion paths was reported.¹ Ion-exchanged MgFeSiO_4 from $\text{Li}_2\text{FeSiO}_4$ exceeds 300 mAh g^{-1} with a reversible magnesium charge/discharge. The full de-intercalation of $\text{Li}_2\text{FeSiO}_4$ or MgFeSiO_4 would presumably result in Fe^{4+} , therefore the charge compensation mechanism was investigated using Fe K-edge X-ray absorption near edge structure (XANES), as shown in Fig. 6(a). The higher and lower energy shifts of the XANES spectra at the Fe K-edge correspond, respectively, to increase and decrease in the oxidation state of the Fe ions, as confirmed in previous iron silicate systems.^{26,27} During the lithium extraction process, a significant shift is observed from $\text{Li}_2\text{FeSiO}_4$ to LiFeSiO_4 . This corresponds to the oxidation of divalent Fe ions to the trivalent state, which is dominated by the outermost orbital of the Fe-3d band. Between LiFeSiO_4 and FeSiO_4 , only a small shift is observed, as has also been noted by others upon a more than one lithium extraction from $\text{Li}_2\text{FeSiO}_4$.²⁶ The small edge shift suggests that other charge compensation mechanisms should be occurring between LiFeSiO_4 and FeSiO_4 . In the subsequent Mg^{2+} (de)insertion processes, reversible shifts in the absorption energies are observed as shown in Fig. 6(b). While the energy shift in the XANES spectrum is small from FeSiO_4 to $\text{Mg}_{0.5}\text{FeSiO}_4$ (similar to what was observed in the LiFeSiO_4 – FeSiO_4 regime), a significant shift is observed from $\text{Mg}_{0.5}\text{FeSiO}_4$ to MgFeSiO_4 . A similar trend was also observed during the magnesium extraction process, as is apparent in Fig. 6(c).

O *K*-edge X-ray absorption spectroscopy (XAS) measurements give further insight for FeSiO_4 (Fig. 6(d)). The pre-edge peak intensity at 529 eV increases as Fe is oxidized; this indicates the degree of hybridization between the Fe 3*d* states and O 2*p* states.²⁸ Such a strong hybridization between the metal and ligand can lead to creation of ligand holes, suggesting this process as the redox mechanism during the charge-discharge reaction of ion-exchanged MgFeSiO_4 . In general, anion redox processes can contribute to large capacities, as has recently been revealed in the lithium (de)intercalation of $\text{Li}_2(\text{Ru},\text{Sn})\text{O}_3$.¹¹ The charge compensation process dominantly occurs within the Fe 3*d* orbital in the $\text{Mg}_{0.5}\text{FeSiO}_4$ – FeSiO_4 regime. Conversely, O 2*p* orbital plays an important role in oxidation/reduction process between $\text{Mg}_{0.5}\text{FeSiO}_4$ and FeSiO_4 regime by creating holes at the ligands.

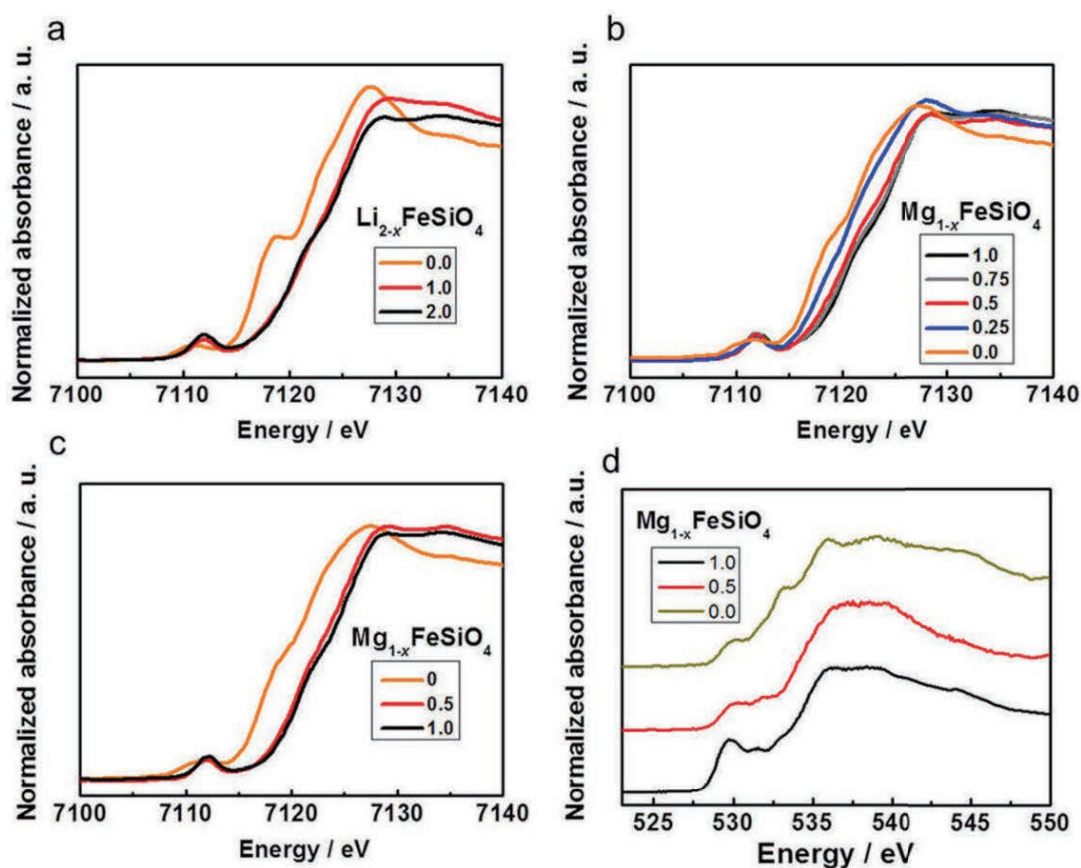


Fig. 6 (a) X-ray absorption near edge structure (XANES) spectra at the Fe *K*-edge of $\text{Li}_{2-x}\text{FeSiO}_4$ during the initial charge (Li^+ extraction) with a Li electrolyte. (b) XANES spectra of $\text{Mg}_{1-x}\text{FeSiO}_4$ during the initial discharge and (c) the initial charge using a Mg electrolyte during Mg^{2+} insertion and extraction, respectively. (d) O *K*-edge XAS spectra of $\text{Mg}_{1-x}\text{FeSiO}_4$ electrode during the initial Mg^{2+} insertion process.¹

The charge compensation mechanism of the ligand-hold type has also been demonstrated in the cathode material of potassium-ion battery. Masse et al. newly synthesized a honeycomb-structured $\text{K}_2\text{Ni}_2\text{TeO}_6$ and reported a reversible charge/discharge of potassium ions.² O *K*-edge XAS measurements were conducted in order to glean, experimentally, information regarding the role of oxygen during potassium-ion extraction/insertion. Although the data were acquired from *ex situ* measurements, caution was taken not to expose the samples to air. Normalised XANES spectra at O *K*-edge of $\text{K}_2\text{Ni}_2\text{TeO}_6$ during electrochemical K-ion extraction/insertion are shown in Fig. 7(a). Galvanostatic measurements reveal a one-electron reaction, thus, the XAS measurements reflect the electronic structural changes occurring within the $\text{K}_2\text{Ni}_2\text{TeO}_6$ – KNi_2TeO_6 regime. A clear variation of the O *K*-edge XAS of the $\text{K}_2\text{Ni}_2\text{TeO}_6$ cathode material before and after charging and discharging was observed. The peak around 532 eV arises from the hybridisation of O-2*p* and Ni-3*d* orbitals, whereas the peak on the high energy side emanates from the hybridisation of O-2*p* orbital and Ni-4*s,p* orbitals.^{9, 29} Emergence of a new peak is discernible at 528 eV (on the low-energy region) upon charging, ascribable to the formation of oxygen ligand hole. This behaviour is in excellent concordance with that observed in Li-excess LiNiO_2 ,¹⁵ LaNiO_3 .³⁰ The peak intensity increase observed at 528 eV, in principle reflects the degree of hybridisation between Ni 3*d*–O 2*p* orbitals, hence we can state that this strength is strongest upon K^+ extraction from $\text{K}_{2-x}\text{Ni}_2\text{TeO}_6$. K^+ extraction leads to the increase in the valency state from $\text{Ni}^{2+} \rightarrow \text{Ni}^{3+}$, the electronic ground state of Ni^{3+} predominantly being 3*d*⁷. However, owing to electronic configuration mixing triggered by the hybridisation with O-2*p* orbitals, the ground state tends to possess a 3*d*⁸ \underline{L} orbital character. Presence in the ground state of this 3*d*⁸ \underline{L} configuration invokes the increase in the pre-edge peak intensity conspicuous at 528 eV upon charging. It is therefore assignable to 3*d*⁸ $\underline{L} \rightarrow \underline{c} d^8$ core transitions and can be rationalised, *vide supra*, as a signature of the hybridisation strength of O 2*p*–Ni 3*d* orbitals. In summary, the trend observed in the O *K*-edge spectra (as was *a priori* revealed by first-principle calculations) signifies that, hybridisation or covalency is large upon potassium extraction from $\text{K}_2\text{Ni}_2\text{TeO}_6$ and vice versa holds.

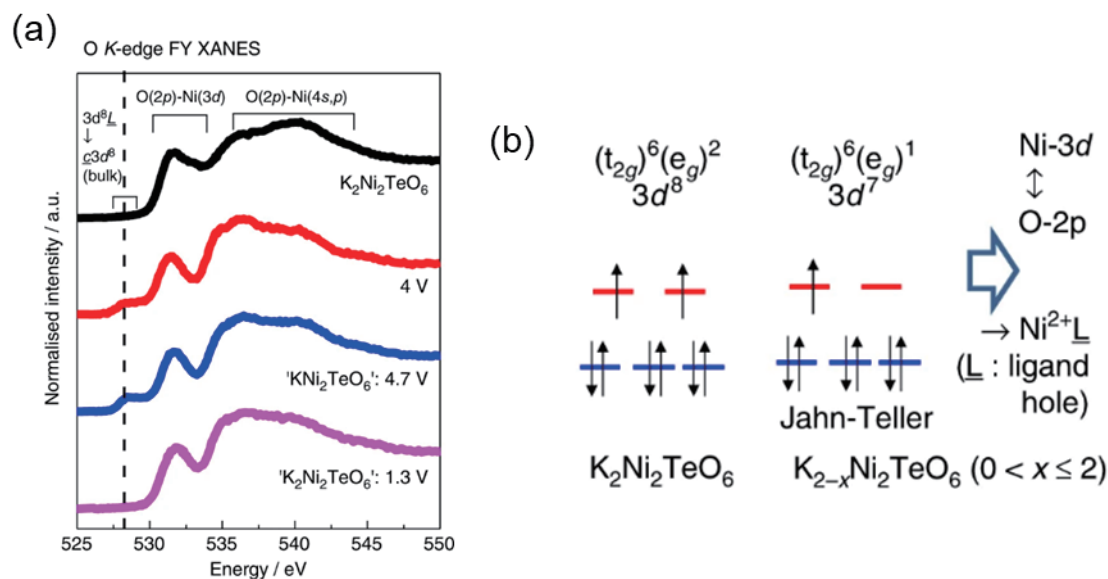


Fig. 7 (a) Normalized O *K*-edge XANES of $\text{K}_2\text{Ni}_2\text{TeO}_6$ cathode during (dis)charging taken in fluorescence yield mode, which is highly sensitive to the innate bulk properties of $\text{K}_2\text{Ni}_2\text{TeO}_6$. Ligand holes are created in the O 2*p* bands during K-ion extraction and vice versa during K-ion reinsertion. (b) Schematic illustration of the electrochemistry of $\text{K}_2\text{Ni}_2\text{TeO}_6$ utilising the ligand hole formation in the hybridised Ni 3*d* and O 2*p* states during K-ion extraction.²

$\text{R}_x\text{MgCl}_{2-x} + \text{R}'_y\text{AlCl}_{3-y}$ ($\text{R}, \text{R}' = \text{n-butyl and/or ethyl}, x = 0-2, y = 0-3$)/THF, developed by Aurbach et al., has dramatically improved performance by showing that^{3, 12} Oxidative Decomposition Potential is wider than that of the conventional Grignard reagent system, that is, the Ion Conductivity is about the same as that of the Li-Ion Secondary Battery Electrolyte, and that Magnesium Dissolution and Precision Response progresses at about 100% coulomb efficiency. In Japan, Wako Pure Chemical Industries has commercialized an electrolytic solution using boron-based magnesium salt as an electrolytic solution for magnesium secondary batteries. Mg *K*-edge XAS can also be applied to an electrolyte solution of a magnesium battery. Measurements are made in a vacuum chamber, but have been made by sealing the solution in the same manner as the cell described earlier.^{24, 31}

Figure 8 (a) shows the Mg *K*-edge XANES of the $\text{B}(\text{OMgCl})_3$ -based electrolytes in triglyme and triglyme-THF. The two main peaks are observed at ~ 1309 and ~ 1312 eV with a shoulder at around 1315 eV. The peak at approximately 1309 eV is attributed to either $[\text{Mg}_2(\mu\text{-Cl})_2]^{2+}$ ³² or $[\text{Mg}_2(\mu\text{-Cl})_3]^+$ species.³³ The position of the main edge at 1312–1315 eV is related to the hexacoordinated solvated structure.^{32, 34} Figure 8 (b) shows the Fourier transform of the Mg *K*-edge extended X-ray absorption fine structure (EXAFS) oscillation of the $\text{B}(\text{OMgCl})_3$ -based electrolyte in triglyme. The Fourier transform for this electrolyte

is closest to those for $\text{Mg}(\text{ClO}_4)_2/\text{H}_2\text{O}$ ³² and $[\text{Mg}_2(\mu\text{-Cl})_3 \cdot 6(\text{THF})]^+$ under applied voltage on the Mg electrode.³³ The peak at around 1.8 Å is expected to contain information about the Mg–O pair. On the other hand, it is unclear whether the peak at 2.6 Å is the scattering peak of the Mg–Mg pair or the peak due to the Mg–Cl pair weakened by triglyme. However, the main edge at 1312–1315 eV in the XANES spectrum and the large peak at 2.6 Å in the EXAFS spectrum indicate that the $\text{B}(\text{OMgCl})_3$ -based electrolytes include more electrochemically positive Mg ion than $[\text{Mg}_2(\mu\text{-Cl})_3]^+$.

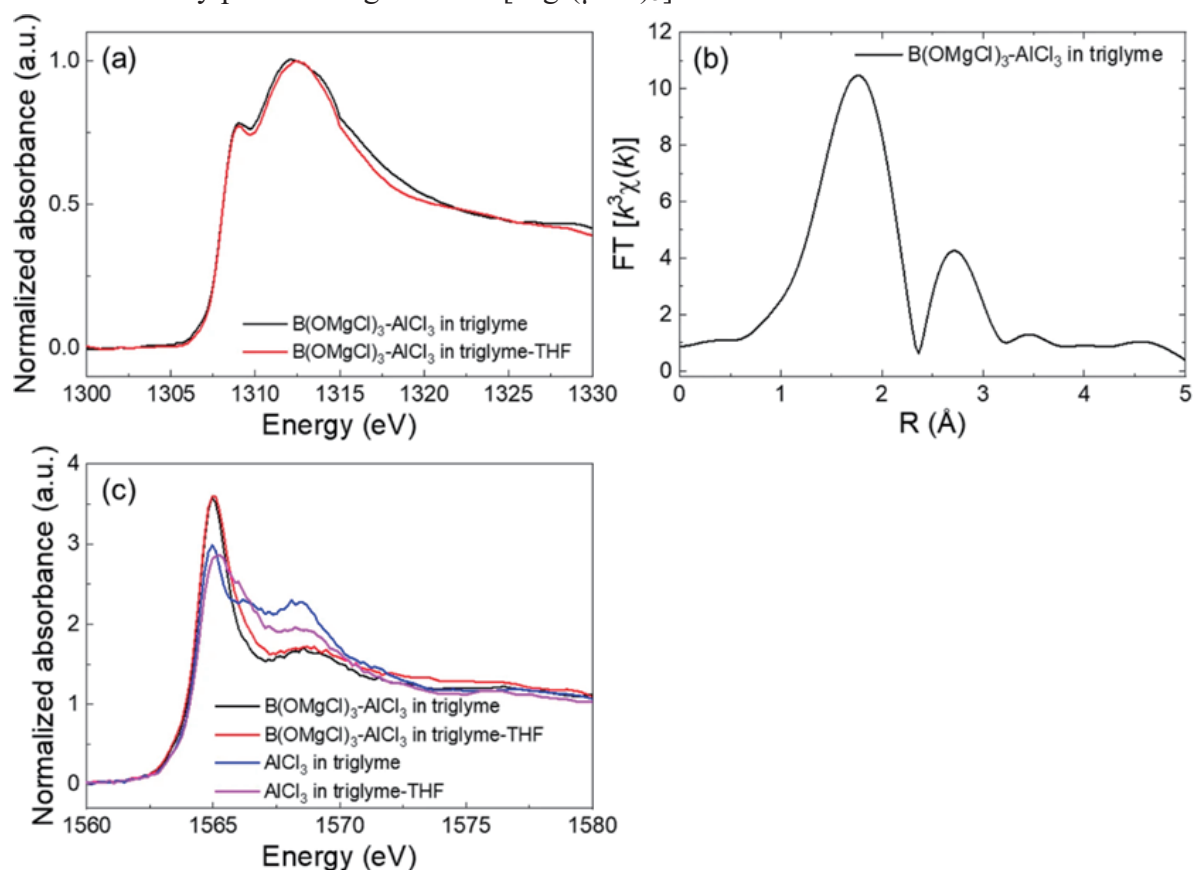


Fig. 8 (a) Mg *K*-edge XANES spectra of $\text{B}(\text{OMgCl})_3\text{-AlCl}_3$ in triglyme (black) and $\text{B}(\text{OMgCl})_3\text{-AlCl}_3$ in triglyme-THF (red) and (b) Fourier transform of the EXAFS function of the former. (c) Al *K*-edge XANES spectra of $\text{B}(\text{OMgCl})_3\text{-AlCl}_3$ in triglyme (black), $\text{B}(\text{OMgCl})_3\text{-AlCl}_3$ in triglyme-THF (red), AlCl_3 in triglyme (blue), and AlCl_3 in triglyme-THF (pink).³

Figure 8(c) represents the Al *K*-edge XANES spectra of the four electrolytes, which are AlCl_3 with or without $\text{B}(\text{OMgCl})_3$ dissolved in triglyme or triglyme-THF. Both AlCl_3 electrolytes without $\text{B}(\text{OMgCl})_3$ in triglyme (blue) and triglyme-THF (pink) show two edges located at 1565 (with a shoulder at around 1566 eV) and 1568 eV. The shoulder at 1566 eV is smaller and the peak at 1568 eV is larger for $\text{AlCl}_3/\text{triglyme}$ compared with those for $\text{AlCl}_3/\text{triglyme-THF}$. These results are consistent with those of ^{27}Al NMR showing

a smaller peak at 62–68 ppm (due to AlCl_3 species) and larger peak at 27 ppm (due to AlCl_2^+ species) for AlCl_3 /triglyme compared with those for AlCl_3 /triglyme-THF. The Al *K*-edge XANES spectra of the AlCl_3 electrolytes with $\text{B}(\text{OMgCl})_3$ show distinctly different absorption curves from those of the AlCl_3 electrolytes without $\text{B}(\text{OMgCl})_3$ in both triglyme and triglyme-THF. The increase of the edge at 1565 eV with the decrease of both the shoulder at around 1566 eV and edge at 1568 eV are consistent with the increase of the amount of AlCl_4^- and decrease of the amounts of both AlCl_3 and AlCl_2^+ observed in the ^{27}Al -NMR measurement. The edge at 1565 eV, shoulder at around 1566 eV, and edge at 1568 eV in the Al *K*-edge XANES spectra are deduced to be related to AlCl_4^- , AlCl_3 , and AlCl_2^+ , respectively.

4. Summary and outlook

Soft X-ray absorption spectroscopy (XAS) has been applied to analyze the reaction mechanism for lithium-ion batteries and next-generation rechargeable batteries. During charge-discharge reaction, redox reaction is happened in electrode active materials. Metal L-edge XAS provides the direct information of redox site. In addition, O *K*-edge XAS is also important because most of the oxide based active materials forms the hybridization state between metal and oxygen orbitals. Operando XAS measurement setup has been developed, which enables to using liquid electrolyte. SXAS of rechargeable batteries is useful to develop next-generation battery materials.

References

- [1] Y. Orikasa, T. Masese, Y. Koyama, T. Mori, M. Hattori, K. Yamamoto, T. Okado, Z. D. Huang, T. Minato, C. Tassel, J. Kim, Y. Kobayashi, T. Abe, H. Kageyama and Y. Uchimoto, *Sci. Rep.*, **2014**, *4*, 5622.
- [2] T. Masese, K. Yoshii, Y. Yamaguchi, T. Okumura, Z.-D. Huang, M. Kato, K. Kubota, J. Furutani, Y. Orikasa, H. Senoh, H. Sakaebe and M. Shikano, *Nature Commun.*, **2018**, *9*, 3823.
- [3] K. Sato, G. Mori, T. Kiyosu, T. Yaji, K. Nakanishi, T. Ohta, K. Okamoto and Y. Orikasa, *Sci. Rep.*, **2020**, *10*, 7362.
- [4] Y. Orikasa, K. Yamamoto, T. Shimizu and Y. Uchimoto, *Chem. Phys. Rev.*, **2022**, *3*, 011305.
- [5] K. Mizushima, P. C. Jones, P. J. Wiseman and J. B. Goodenough, *Mater. Res. Bull.*, **1980**, *15*, 783.
- [6] J. B. Goodenough and Y. Kim, *Chem. Mater.*, **2010**, *22*, 587.

- [7] P. Ghigna and E. Quartarone, *J. Phys. Energy*, **2021**, 3, 032006.
- [8] I. Nakai, K. Takahashi, Y. Shiraishi, T. Nakagome and F. Nishikawa, *J. Solid State Chem.*, **1998**, 140, 145.
- [9] Y. Uchimoto, H. Sawada and T. Yao, *J. Power Sources*, **2001**, 97-98, 326.
- [10] M. M. Thackeray, S.-H. Kang, C. S. Johnson, J. T. Vaughey, R. Benedek and S. A. Hackney, *J. Mater. Chem.*, **2007**, 17, 3112.
- [11] M. Sathiya, G. Rouse, K. Ramesha, C. P. Laisa, H. Vezin, M. T. Sougrati, M. L. Doublet, D. Foix, D. Gonbeau, W. Walker, A. S. Prakash, M. Ben Hassine, L. Dupont and J. M. Tarascon, *Nature Mater.*, **2013**, 12, 827.
- [12] M. Sathiya, A. M. Abakumov, D. Foix, G. Rouse, K. Ramesha, M. Saubanère, M. L. Doublet, H. Vezin, C. P. Laisa, A. S. Prakash, D. Gonbeau, G. VanTendeloo and J. M. Tarascon, *Nature Mater.*, **2015**, 14, 230.
- [13] N. Yabuuchi, M. Takeuchi, S. Komaba, S. Ichikawa, T. Ozaki and T. Inamasu, *Chem. Commun.*, **2016**, 52, 2051.
- [14] N. Yabuuchi, M. Nakayama, M. Takeuchi, S. Komaba, Y. Hashimoto, T. Mukai, H. Shiiba, K. Sato, Y. Kobayashi, A. Nakao, M. Yonemura, K. Yamanaka, K. Mitsuhara and T. Ohta, *Nature Commun.*, **2016**, 7, 13814.
- [15] M. Oishi, T. Fujimoto, Y. Takanashi, Y. Orikasa, A. Kawamura, T. Ina, H. Yamashige, D. Takamatsu, K. Sato, H. Murayama, H. Tanida, H. Arai, H. Ishii, C. Yogi, I. Watanabe, T. Ohta, A. Mineshige, Y. Uchimoto and Z. Ogumi, *J. Power Sources*, **2013**, 222, 45.
- [16] M. Oishi, K. Yamanaka, I. Watanabe, K. Shimoda, T. Matsunaga, H. Arai, Y. Ukyo, Y. Uchimoto, Z. Ogumi and T. Ohta, *J. Mater. Chem. A*, **2016**, 4, 9293.
- [17] M. Oishi, C. Yogi, I. Watanabe, T. Ohta, Y. Orikasa, Y. Uchimoto and Z. Ogumi, *J. Power Sources*, **2015**, 276, 89.
- [18] K. Luo, M. R. Roberts, R. Hao, N. Guerrini, D. M. Pickup, Y.-S. Liu, K. Edström, J. Guo, A. V. Chadwick, L. C. Duda and P. G. Bruce, *Nature Chem.*, **2016**, 8, 684.
- [19] D.-H. Seo, J. Lee, A. Urban, R. Malik, S. Kang and G. Ceder, *Nature Chem.*, **2016**, 8, 692.
- [20] N. Yabuuchi, M. Takeuchi, M. Nakayama, H. Shiiba, M. Ogawa, K. Nakayama, T. Ohta, D. Endo, T. Ozaki, T. Inamasu, K. Sato and S. Komaba, *Proc. Natl. Acad. Sci. U.S.A.*, **2015**, 112, 7650.
- [21] K. Nakanishi, D. Kato, H. Arai, H. Tanida, T. Mori, Y. Orikasa, Y. Uchimoto, T. Ohta and Z. Ogumi, *Rev. Sci. Instrum.*, **2014**, 85, 084103.
- [22] K. Yamamoto, Y. Zhou, N. Yabuuchi, K. Nakanishi, T. Yoshinari, T. Kobayashi, Y. Kobayashi, R. Yamamoto, A. Watanabe, Y. Orikasa, K. Tsuruta, J. Park, H. R. Byon, Y. Tamenori, T. Ohta and Y. Uchimoto, *Chem. Mater.*, **2020**, 32, 139.

- [23] C. Yogi, D. Takamatsu, K. Yamanaka, H. Arai, Y. Uchimoto, K. Kojima, I. Watanabe, T. Ohta and Z. Ogumi, *J. Power Sources*, **2014**, 248, 994.
- [24] D. Aurbach, Z. Lu, A. Schechter, Y. Gofer, H. Gizbar, R. Turgeman, Y. Cohen, M. Moshkovich and E. Levi, *Nature*, **2000**, 407, 724.
- [25] P. Canepa, G. Sai Gautam, D. C. Hannah, R. Malik, M. Liu, K. G. Gallagher, K. A. Persson and G. Ceder, *Chem. Rev.*, **2017**, 117, 4287.
- [26] D. P. Lv, J. Y. Bai, P. Zhang, S. Q. Wu, Y. X. Li, W. Wen, Z. Jiang, J. X. Mi, Z. Z. Zhu and Y. Yang, *Chem. Mater.*, **2013**, 25, 2014.
- [27] R. Dominko, C. Sirisopanaporn, C. Masquelier, D. Hanzel, I. Arcon and M. Gaberscek, *J. Electrochem. Soc.*, **2010**, 157, A1309.
- [28] A. Augustsson, G. V. Zhuang, S. M. Butorin, J. M. Osorio-Guillén, C. L. Dong, R. Ahuja, C. L. Chang, P. N. Ross, J. Nordgren and J.-H. Guo, *J. Chem. Phys.*, **2005**, 123, 184717.
- [29] L. Sanchez and J.-P. Pereira-Ramos, *J. Mater. Chem.*, **1997**, 7, 471.
- [30] M. Abbate, G. Zampieri, F. Prado, A. Caneiro, J. M. Gonzalez-Calbet and M. Vallet-Regi, *Phys. Rev. B*, **2002**, 65, 155101.
- [31] D. Aurbach, H. Gizbar, A. Schechter, O. Chusid, H. E. Gottlieb, Y. Gofer and I. Goldberg, *J. Electrochem. Soc.*, **2002**, 149, A115.
- [32] Y. Nakayama, Y. Kudo, H. Oki, K. Yamamoto, Y. Kitajima and K. Noda, *J. Electrochem. Soc.*, **2008**, 155, A754.
- [33] A. Benmayza, M. Ramanathan, T. S. Arthur, M. Matsui, F. Mizuno, J. Guo, P.-A. Glans and J. Prakash, *J. Phys. Chem. C*, **2013**, 117, 26881.
- [34] M. Hattori, K. Yamamoto, M. Matsui, K. Nakanishi, T. Mandai, A. Choudhary, Y. Tateyama, K. Sodeyama, T. Uchiyama, Y. Oriyasa, Y. Tamenori, T. Takeguchi, K. Kanamura and Y. Uchimoto, *J. Phys. Chem. C*, **2018**, 122, 25204.